Multispectral 2D Imaging for Oxygen Saturation in Tumor Detection

Chengxi Fan, Yining Guo, Ziwen Xie

Group # 22

Advisors: Ousama A'Amar, Irving Bigio

Department of Biomedical Engineering
Boston University

April 16, 2021

Abstract

Tumors exhibit greater vascularization and lower blood oxygenation. Suspicious tumors may be detected by measuring the changes in oxygen saturation (SO_2), noninvasively. In this project, we explore a method to perform 2D SO_2 mapping of superficial human tissue. Oxygenated and deoxygenated hemoglobin exhibit distinctive reflection patterns of light in response to both red and near-infrared (NIR) wavelengths. Using a multispectral imaging technique, SO_2 mapping of a region of interest (ROI) can be performed. Light from red and NIR LEDs is sequentially projected on tissue while the image sequence is automatically recorded. Frames are then isolated and processed at each illumination wavelength. LEDs are placed at a specific angle relative to the surface of the tissue so that the camera only captures reflected light that interacts with the targeted tissue. The frames are then analyzed with an algorithm that was designed to extract and process the light intensities frame by frame. Each frame is split into 10X10 pixels areas. The average intensity of each area is collected over time. Matching pixel coordinates are then used to produce SO_2 maps. Both the device and the algorithm are validated by liquid phantoms that mimic the optical properties of oxygenated and deoxygenated tissues. Consequently, our product, utilizing 2D SO_2 imaging technology, is capable of producing high-resolution images of SO_2 mapping from targeted tissues based on the difference in vascularization.

1.0 Introduction & Background

As one of the most common leading causes of death in the world, cancer leads around 10 million deaths worldwide in 2020. The high growth rate and rapid deterioration of cancer make tumor detection at an early stage an essential task. In general, early diagnosed cancer has a greater opportunity for recovery[10]. Some cancer diagnostic technologies such as endoscopy are invasive[11], and traditional diagnostic methods like whole-body CT and MRI have disadvantages including radiation exposure, high cost, non-routine basis, and potentially low yield in detecting significant abnormalities in these patients[5,13]. As such, any more effective and economic early detection innovation is lifesaving.

Oxygen saturation measurement provides a good way of visualizing suspicious tumor tissue[12,14]. Point measurement method of SO_2 level like pulse oximetry is well-studied in nowadays research. The method makes use of photoplethysmographic pulses in the red and infrared regions and employs the concept from the absorption spectra of hemoglobin[6,7,8,9]. When the wavelength of light shining on tissue surface is larger than 800 nm (the isobestic point), the extinction coefficient of oxygenated hemoglobin (HbO_2) is higher, which means that more of the light will get absorbed by it, compared to that in deoxygenated hemoglobin (Hb); vice versa, when the wavelength of light is smaller than 800 nm, deoxygenated hemoglobin shows a greater absorption level than oxygenated hemoglobin. This property of absorption spectra enables us to differentiate tumor and healthy regions on a tissue surface by mapping the intensity of light reflected back from hemoglobin-sufficient tissue surface.

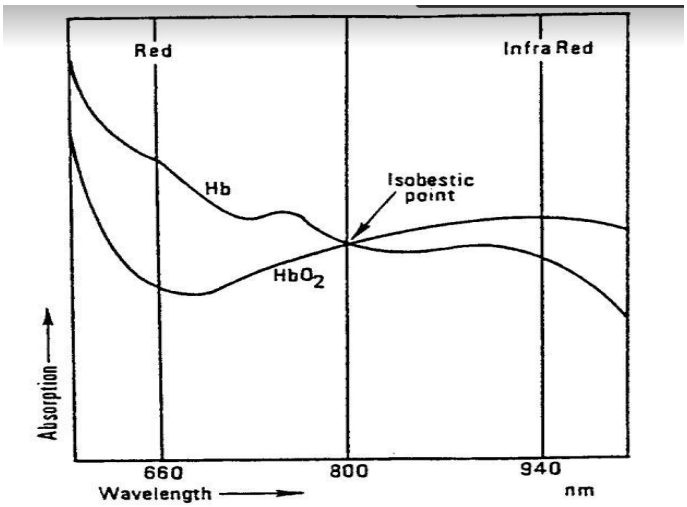


Figure 1. Absorption spectra Hb and HbO_2 (the isobestic point is the wavelength at which the absorption by the two forms of the molecule is the same). Figure reproduced from *Neil Townsend, 2001*.

The benefit of this application is that it is noninvasive and without the use of radiation exposure, while the disadvantage is apparent, in that it doesn't increase the accuracy of cancer detection: measured SO_2 levels can differentiate by a large degree from the actual value due to light scattering effect[6,16,17]. In recent studies, a 2D optical device that provides a two-dimensional mapping of HbT and SO_2 in human tissue can reach as much as 92% diagnostic sensitivity and 67% specificity in detecting ductal carcinoma[2]. This supports that 2D imaging for SO_2 in biological tissues may also improve current detection accuracy in other types of cancerous tissues, for instance, if 2D imaging for SO_2 can be combined with invasive detection methods like endoscopy[14,18]. Furthermore, the 2D optical device has a potential commercial value since its portability compared to the traditional radiation detection method allows it to reach out to non-governmental organizations and markets with low-resource medical settings[15].

Current oxygen saturation measurement methods like pulse oximetry are common in clinical use[6,7,8,9]. However, the pulse oximetry only accounts for an estimation of arterial blood SO_2 over a small area, while few applications are made in observing the distribution of SO_2 level over a larger area of biological tissue. Although the idea of 2D mapping is well-researched[12], it hasn't developed to application in tumor detection circumstances.Thus, 2D mapping in our project can challenge current clinical practice paradigms by allowing clinicians to record and visually observe the abnormalities in cancer-risky regions that traditional pulse oximeters cannot. Also, the design is innovative since it captures the light interacted and reflected back from the skin surface, rather than collects the light transmitted through one's fingertip. In this case, the design brings the image collector and the light emitter to the same side of the model, allowing the device to directly sit on the

targeted tissue surface. Unlike a pulse oximeter, which requires a finger clip and is limited to point measurement on the fingertip, our design can be applied to various skin surfaces. Moreover, the design gives a more convenient and prompt way of cancer screening in health examinations. A set of algorithms is compiled for the image processing, calculating a 2D image for oxygen saturation distribution, and a graphical user interface (GUI) is constructed for the convenience of users. The algorithms also allow users to modify and update the system of 2D mapping analysis easily in the future. In addition, the circuit design of the device enables users to utilize GUI to interact with the LEDs. A metal-oxide semiconductor field-effect transistor (MOSFET) is included in the circuit to control the main parameters, which are resistance and a switch that can turn on or off the lights of the circuit. The circuit also contains LEDs with two different wavelengths of light, which are 624 nm for red lights and 640 nm for NIR lights, inserted in the scanning device alternatively. Therefore, the entire system provides a user-friendly way to switch between light sources and simplifies the measurement process.

In addition, the project utilized optical phantoms for device validation. The self-designed liquid phantoms mimic the optical properties of human superficial tissue and are able to test the system for its accuracy of SO_2 level. The successful validation of our designed device via such method would allow further research and development and hence commercialization and clinical use.

2.0 Methods

2.1 Preliminary Experimental Design

The idea of our design is based on a well-established mechanism of pulse oximetry; therefore, we first tested this knowledge into practice by observing the process of light transmission through our superficial tissue, which was the skin on our hands. The video preliminary experiment was used to prove that proper images could be captured and analyzed through reflection. The goal of this stage was to identify the cardiac pulse rhythms from the recorded video over the skin of the fingertip. The devices involved in this preliminary experiment included a mobile phone camera, a hand-built simple camera holder made by a card box, LEDs in different wavelengths, which were the red lights with a wavelength of 624 nm and the NIR lights with a wavelength of 880 nm, jumper wires, and a circuit breadboard for building the LED setups. We used a jumper wire to connect a red-light LED to a resistor in series so that the power dissipated on the LED did not exceed the maximum. Then we applied a voltage source to the circuit and placed the finger on the top of the LED so that the red light was transmitted and could be viewed through the tissue. Finally, we recorded a video of the fingertip for 10 seconds, read the video file in MATLAB, and selected a 10×10 region in pixels as the area of interest for calculation of the average intensity of light in the chosen region.

2.2 Imaging Acquisition Device

2.2.1 Overview of Imaging Acquisition Device

The proposed device contains an imager with a central hole for camera measurement and a ring of holes that LEDs can be inserted in. There are 12 LED inserting spots for six 940-nm NIR LEDs and six 624-nm red LEDs. The LEDs are controlled from a circuit that connects to a Raspberry Pi to switch automatically and generate lights with different wavelengths. The camera receives image information when the targeted tissue is illuminated by the desired wavelength of light.

The mapping device was started with multi-pronged strategies as described in Figure 2. The initial design was an imager with a central coherent optical fiber bundle. A camera was attached to the fiber bundle via the camera holder that kept the camera at a desired distance of its focal length from the fiber bundle; measurements through this optical fiber bundle were directly attached to the target tissue, which might lack feasibility. An alternative approach was developed to have the Pi Camera be directly attached to the imager, as shown in Figure 2 (B). The tilted angle of the LED pathway needed to be carefully calculated to get an effective feedback to the camera using the angle model described in Section 2.2.2. Figure 2(C) shows another modification of the design: instead of LEDs being inserted into the hole, optical fibers were used to deliver lights to the tissue through a connector. Glass fibers were chosen to be the optical material due to its strength and flexibility. A great advantage of this fiber was that it was able to deliver the light source from one terminal to another coherently regardless of its bending.

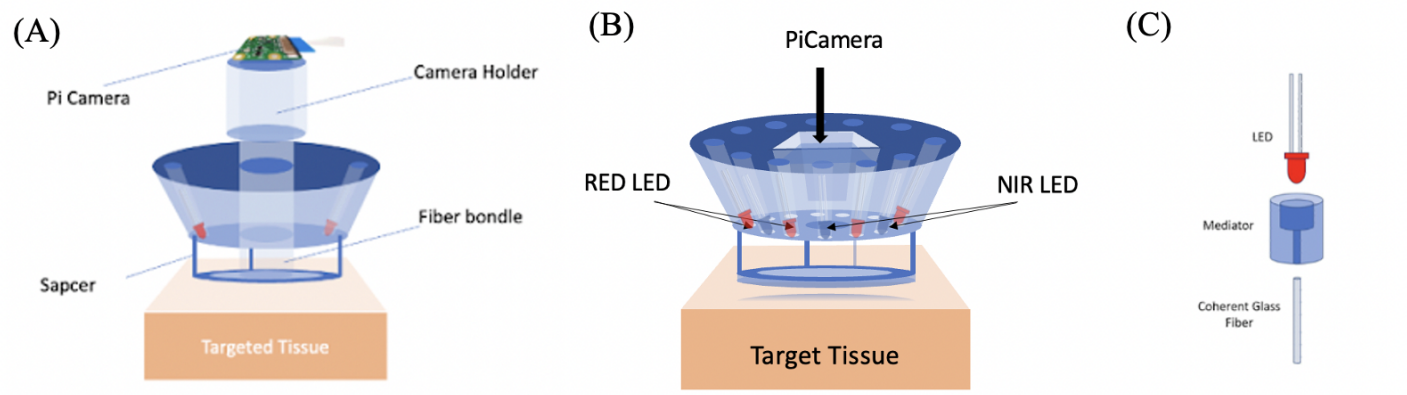


Figure 2. The three approaches for device design. **(A)** The SO_2 mapping device with central coherent optical fiber bundle; **(B)** SO_2 mapping device without optical fiber; **(C)** The modification of SO_2 mapping device with peripheral coherent optical fibers.

The final design focused on the mapping device without optical fibers. A detailed design schematic is described in Figure 3. The imager was modeled using Solidworks and 3D-printed using Creality Ender 3 V2. The model is then assembled with LEDs and camera. The camera used in this prototype was Raspberry Pi Camera Module v2, with 8MP Sony IMX219 image sensor, which was able to detect infrared light. The depth of field was adjusted by a 3D printed tool to reach a focal length of 24 mm[28]. The camera was connected to the Raspberry Pi via the camera port and sample tests were carried out to ensure the functionality of the device. A Graphical User Interface(GUI) was developed on the Raspberry Pi using PythonTkinter to control the camera and LEDs. After the button "Start Recording" was clicked, the device would capture an image of the target tissue with no illumination. Then the six red lights would be turned on and a sequence of 300 images with 60 frames per second would be quickly captured through the video port of the camera. The red lights stopped after collection, and then NIR lights illuminated the area with the same number of images being captured and stored into a different folder. The captured images were analyzed both directly through the Raspberry Pi and through MATLAB, given that the mapping process would take a rather long time in Raspberry Pi . As a result, a SO_2 mapping would be produced as the output.

The device was first designed and tested using a breadboard, and then assembled into a container. The imager sat on the bottom level, with the spacer extruded to keep focal length, Raspberry Pi sat on the next level, battery and control circuits sat on the top level.

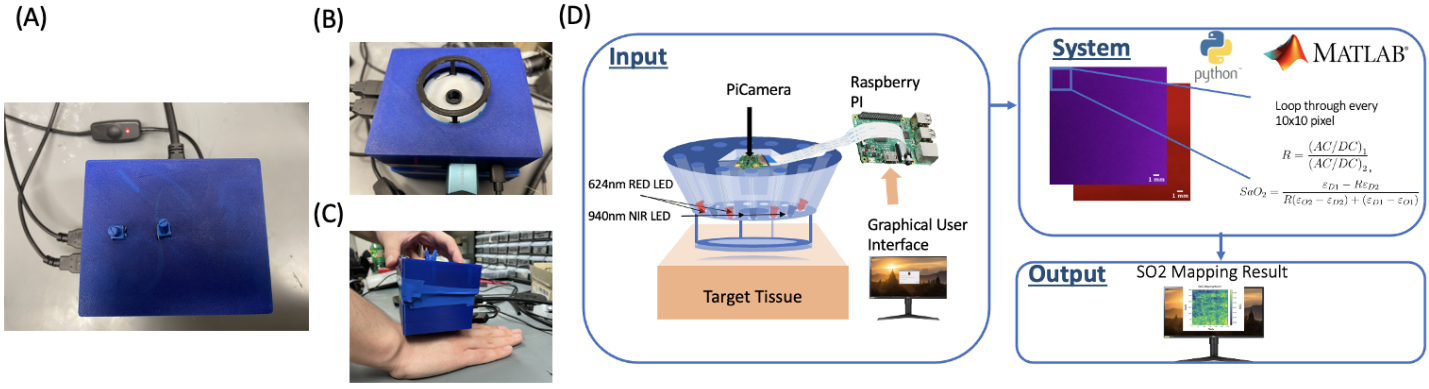


Figure 3. The final design. **(A)** The button with red light at the top is used to control the on/off of Raspberry Pi and the rotary knobs are used to adjust red and NIR light intensity **(B)**The bottom view of the design, a spacer is extruded out to keep focal distance. **(C)** The device under use. **(D)** The schematic plot of the device.

2.2.2 Angle Model

To ensure that the reflected specular light interference would have no effect on the final image, the angles of the inserted LEDs needed to be calculated. The aim was to capture light that interacts with the target tissue. However, if the LED angle were not directed as shown in Figure 4 (B), the reflected specular light

interference would have entered the camera, causing the image intensity to saturate and hence leads to inaccuracy in image measurement.

The goal of the mapping device was to guarantee that only the diffused light can be captured by the camera. The ideal case is illustrated in Figure 4 (C). A geometric model was built accordingly using Geogebra to find appropriate . with three parameters, indicating the angle range, as shown in figure(2).

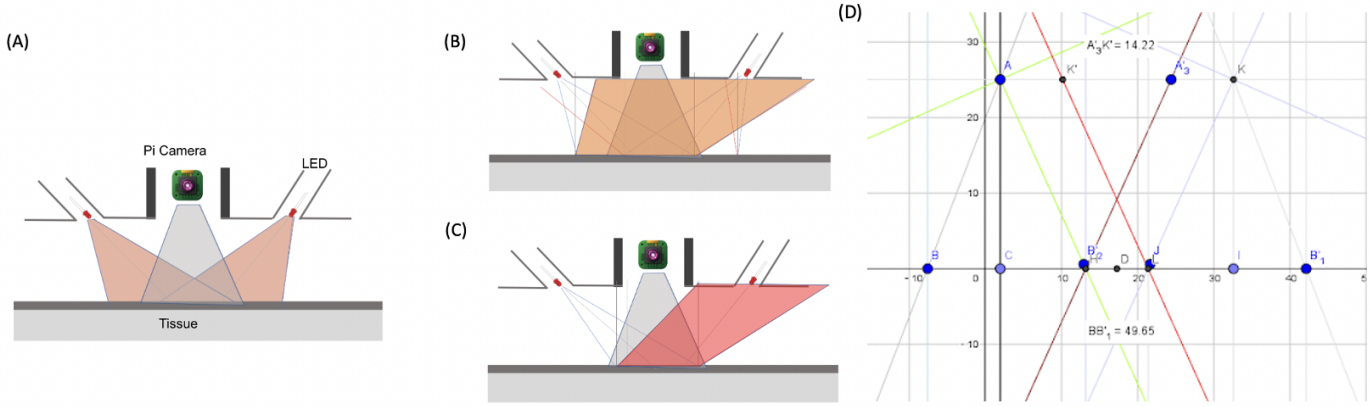


Figure 4 - The angle model. **(A)** The incoming LED light path. **(B)** Case of which the reflected lights directly enter the camera. **(C)** Case of which the reflected lights avoid the direct entry of the camera. **(D)** The Geometric model built in GeoGebra. The three key parameter are: (1) AC: Camera Focal Length. (2) ∠CAB: tilted angle. (3) A3'K': distance from camera hole.

2.2.3 Circuit Design

The circuit design aims to allow users to control the on and off of light with different wavelengths independently using GPIO output, and tune the brightness of LEDs. The idea of the circuit design adopts metal-oxide semiconductor field-effect transistors (MOSFET). According to Figure 5, an external 9V power source gives supply voltage to the whole circuit, and LEDs with the same wavelengths are connected parallelly. A potentiometer is also connected in series with other components to adjust the total resistance of the circuit, which in turn varies the brightness of LED. An N-channel transistor is connected to both the main circuit and the GPIO output from Raspberry Pi, where it acts like a switch that determines whether the circuit is open or closed. Finally, the GPIO pin in conjunction with the transistor acts as a signaling input that triggers the switch.

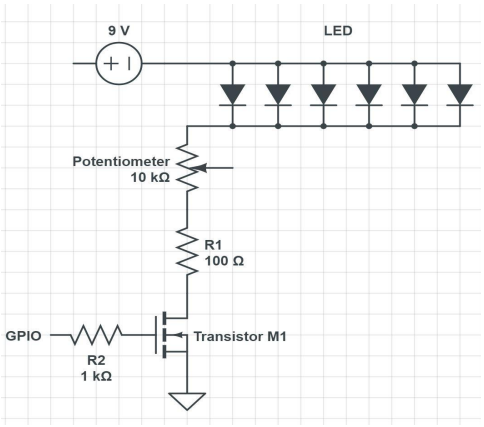


Figure 5. MOSFET circuit design.

2.2.4 GUI

A GUI is developed using python on the Raspberry Pi. It consists of several functions: **(1) Image preview:** Once the GUI is executed, it displays the preview of the camera imaging area **(2) Start recording:** After clicking the start recording button, the program will start, LEDs are switched on and off and image sequence will be recorded. **(3) LED control**: The red LEDs and NIR LEDs can be turned on for testing purposes. **(4) Save data**: The data can be saved into a separate folder **(5) Analyze:** After clicking the plot signal button the signal can be plotted, after clicking the mapping button the SO_2 mapping will be produced. **(6) Camera control:** The sliders can control the properties of the cameras including the exposure time and intensity level. The intensity level is controlled using pulse width modulation (PWM), that user can input specific intensity level.

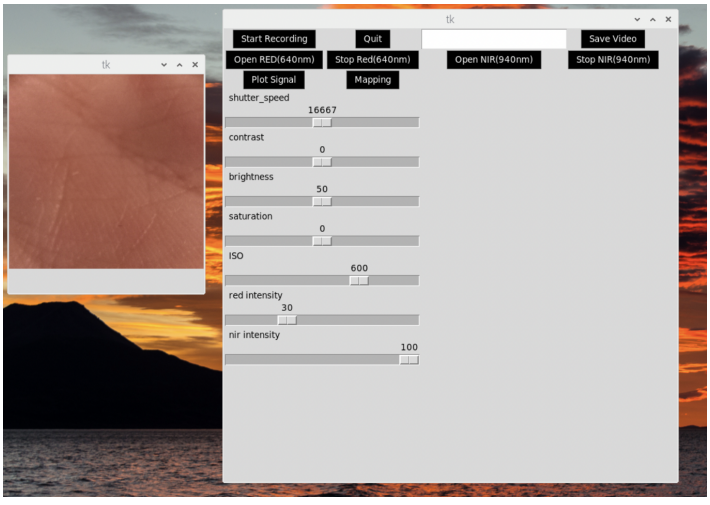


Figure 6. GUI on the screen of the Raspberry Pi. Left: camera preview of hand under the white light; Right: control panel.

2.3 Computational Method

The approach of data collection is reflection, and two wavelengths of light are used, which are 624 nm for the red lights and 940 nm for the NIR lights. The image sequence is captured rapidly for 5 seconds in a completely dark environment by a Pi Camera attached to a Raspberry Pi with the sample, which is the skin, to be stationary. The total number of images for each sequence is 300. Two sets of image sequences are captured, each of which is for each wavelength and has 5 seconds. After data collection, the image data is then taken to Python for generation of SO_2 mapping. The starting region for analysis is the upper left corner consisting of 10×10 in pixels. The algorithm first reads each image sequence, analyzes the light intensity of the data, and outputs a corresponding plot. This plot is used to validate the algorithm via the observation of which the pattern resembles the heart rate pattern. The light intensity data can be further used for the calculation of SO_2 in the selected region.The red and the NIR data are in parallel via the alignment of the first local minima. For the calculation of SO_2 using light intensity, we use the equation

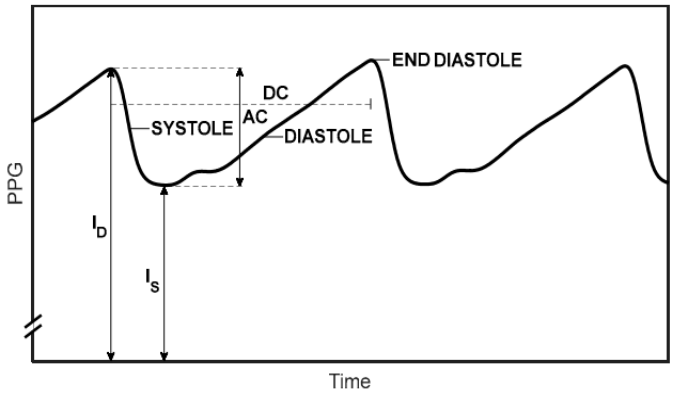


Figure 7. The photoplethysmography (PPG) pulses. AC is the difference between the maximal (I_D) and minimal (I_S) light transmission through the tissue; DC is the mean light transmission through the pulse. *Figure reproduced from Hay, 2018.*[6]

$$R = \alpha \frac{(AC/DC)_1}{(AC/DC)_2} \qquad (1)$$

where *AC* and *DC* are presented in Figure 6[6]. The subscripts 1 and 2 refer to the red light and the NIR light in each pair, respectively. The constant *α* is a simple calibration factor that adjusts the difference between the device and the actual SaO_2 using a pulse oximeter. With the obtained *R* value, the equation

$$SaO_2 = \frac{\varepsilon_{D1} - R\varepsilon_{D2}}{R(\varepsilon_{O2} - \varepsilon_{D2}) + (\varepsilon_{D1} - \varepsilon_{O1})} \qquad (2)$$

is implemented to calculate the SO_2 of the selected region. In the equation, ε_O and ε_D are the molar extinction coefficients of oxyhemoglobin and deoxyhemoglobin, respectively, at a specific wavelength indicated as the number in the subscript, which are all given[6]. Finally, in order to obtain the SO_2 mapping of the entire region of interest, the algorithm loops through every 10×10-pixel area via those processes. An alternate algorithm was additionally designed in MATLAB for verification of the mapping through the same processes.

2.4 Optical Phantoms

For the validation of the designed device, two liquid phantoms, simulating two different levels of SaO_2,were developed to check if our device would be able to successfully detect the difference between them. Phantoms were created based on the compounds shown in Table 1. The base of the phantoms was designed to mimic the properties of the superficial tissue, which was validated by checking if it has approximately identical spectrum with the one from the human finger, via the BMO Gen-4



Figure 8. Liquid phantoms. Left: mimicking tissue with less SaO_2; Middle: mimicking tissue with normal level of SaO_2; Right: the base of phantoms.

spectrometer. Figure 7 presents the final products of the phantoms, whose difference in concentrations would be used to test if our designed device were able to differentiate.

Table 1. Chemical composition of the phantoms.

Base of the phantoms	Phantom mimicking the tissue with the normal level of SaO_2	Phantom mimicking the tissue with less SaO_2
0.5 g TiO_2, 666 mL water	30 mL of the base, 300 μL red dye	30 mL of the base, 300 μL red dye, 150 μL green dye

2.5 Noise Measurement

A noise measurement was made to determine the noise level of our signal. Background noise and dark noise were measured. The background noise was measured with the camera facing on a piece of black fabric, so that minimum amount of light is reflected back, while the dark noise was measured with the camera facing the air with no light reflection. The Signal to Noise Ratio(SNR) is calculated using signal and background noise using equation (3), where A is the mean-square root of the signal.

$$SNR = \frac{P_{signal}}{P_{noise}} = \left(\frac{A_{signal}}{A_{noise}}\right)^2 \quad (3)$$

3.0 Results

3.1 Noise Measurement

In order to calculate the noise, 3 test runs were performed for each type of noise. Since cameras have different sensitivity to each type of noise, both NIR and RED were tested. The background noise of the Red light is 5.33% to the entire signal range and the NIR light has 7.24%, respectively. The result is shown in Table 2. The SNR of the Red light and NIR light was also calculated correspondly using equation (3). The SNR of the NIR signal is 24.6 dB, the SNR of the Red signal is 26.9 dB.

Table 2. Measurements of noise.

			Mean		Standard Deviation	Error Level	
Background Noise	RED	Test1	12.895	13.637	0.208	5.04%	5.33%
		Test2	12.469		0.251	4.87%	
		Test3	15.546		0.735	6.07%	
	NIR	Test1	18.457	18.522	0.686	7.21%	7.24%
		Test2	18.445		0.410	7.21%	
		Test3	18.664		0.264	7.29%	
Dark Noise	RED	Test1	0.998	0.998	0.003	0.39%	0.39%
		Test2	0.998		0.003	0.39%	
		Test3	0.999		0.001	0.39%	
	NIR	Test1	0.997	0.994	0.006	0.39%	0.39%
		Test2	0.999		0.002	0.39%	
		Test3	0.984		0.022	0.38%	

3.2 Phantom Validation

With the phantom designed, images were taken with our designed device. The mean intensity of the phantom was recorded in Table 3, with red and have a higher intensity in the oxygenated phantom and NIR have a

higher intensity at deoxygenated phantom.

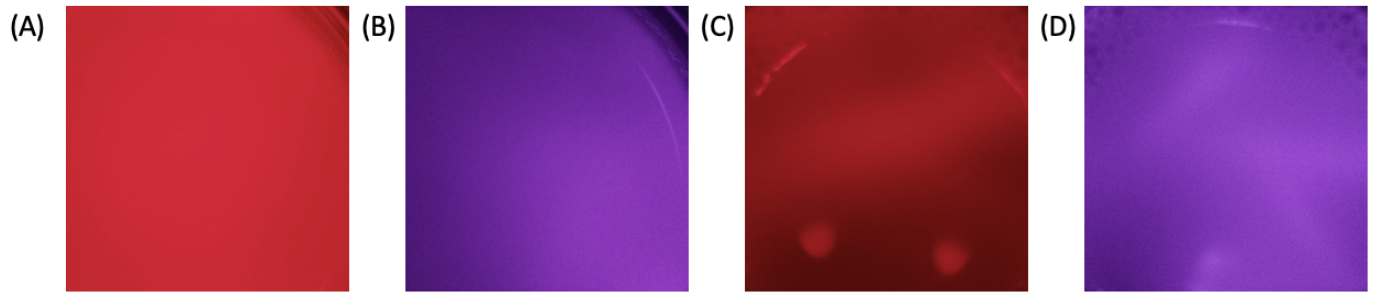


Figure 9. Images of the phantom taken by the mapping device. **(A)** Image of the oxygenated phantom under 624nm red LED light. **(B)** Image of the oxygenated phantom under 940nm red LED light. **(C)** Image of the deoxygenated phantom under 624nm red LED light. **(D)** Image of the deoxygenated phantom under 624nm red LED light.

Table 3. Mean intensity of the phantom.

	Phantom type	**LED Type**	
		Red	NIR
Mean Intensity	Oxygenated	89.293	80.391
	deoxygenated	70.805	82.333

3.3 Computational Results

The designed algorithm in MATLAB first read two sets of image sequence data, whose first images are presented in Figure 9, and then produced a light intensity plot for each wavelength of light, as shown in Figure 10. The original plots appeared to consist of too much noise, which led to the application of a low pass filter with a cutoff frequency of 2 Hz that removed the noise and further resulted in cleaner signals. The plots in Figure 10 both exhibit sinusoidal waves that resemble the signal of heart rate with a consistent frequency of approximately 72 Hz, or 72 heart beats per minute (bpm). With the acquired local maxima and local minima

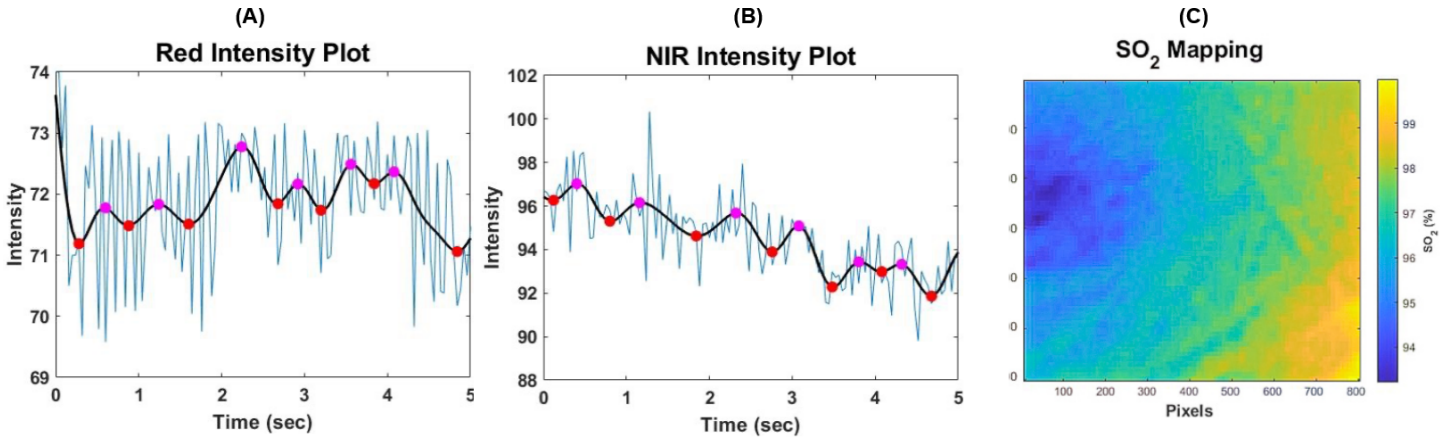


Figure 10. Light intensity plots of the upper left corner of the captured image. **(A)** Wavelength: 624 nm **(B)** Wavelength: 940 nm. **(C)** Mapping result produced by MATLAB. The purple dots refer to the local minima, and the red dots refer to the local minima for plots (A) and (B).

from plots (A) and (B) in Figure 10, the algorithm proceeded to Equations (1) and (2) for every area to generate the SaO_2 mapping of the entire captured region. As a result, as presented in Figure 10 (C), the SaO_2 values range from 93% to 100%.

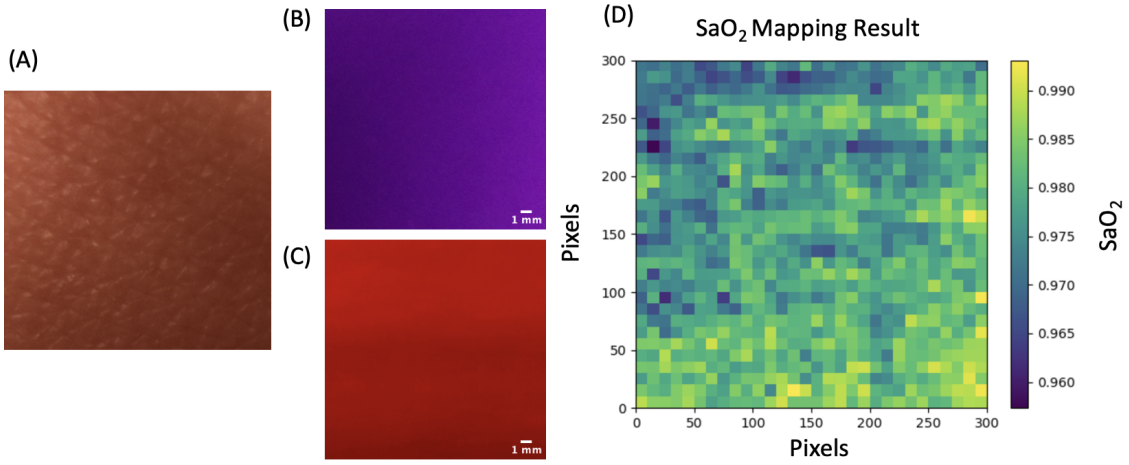


Figure 11. Mapping results produced by Python. The dimension of the captured image is 300×300 in pixels. **(A)** The raw picture under natural white light. **(B)** The raw picture with 940-nm NIR lights. **(C)** The raw picture with 624-nm red lights. The red uses a wavelength of 624 nm, and the NIR uses a wavelength of 940 nm. The purple dots refer to the local minima, and the red dots refer to the local minima for each plot. **(D)** The final mapping result.

The algorithm in Python also proceeded the same process as above but with a different set of image sequences, which produced Figure 11 (D), presenting a SaO_2 range from 95% to 100%.

4.0 Discussion

The results in section 3.1 show that both the error level of the background noise and the dark noise is within acceptable limits (<10%). This proves that our captured image intensity was moderately interfered by these types of noises. By applying a low-pass filter with 2Hz cutoff frequency, noises can be reduced and the filtered data is able to provide reasonable results.

Based on Table 3, the mean intensity of the images of phantoms captured under our device proves the proposed theory and validify our device. When the phantoms are exposed to red light with 624 nm, the phantom that mimics tissue with normal oxygenation has a greater intensity than the one that mimics tissue with lower oxygenation. Vice versa when the phantoms are exposed to NIR light with 940 nm, the phantom that mimics tissue with lower oxygenation has a greater intensity than the one that mimics tissue with higher oxygenation. The generated results are coherent with the theoretical expectation based on the absorption spectra of hemoglobin.

By viewing the intensity plots shown in Figure 10, both the red and the NIR light intensity signals exhibit sinusoidal heart rate patterns with a uniform frequency of approximately 72 Hz, which means that the captured signals corresponds to pulsive fluctuations, and our filtered data are qualified for further calculations in oxygen saturation. In Figure 11, the image sequences processed by Python result in SaO_2 values ranging from 95% to 100%, which matches the normal level of SaO_2 in the scholarly work of Peterson[27], while those processed by MATLAB result in slightly lower values and a wider range of SaO_2, as presented in Figure 10 (C), indicating a potential limitation of our designed device.

Despite the positive results obtained by our device, limitations still exist in our design, and further experiments need to be done. First, one possible reason that Figure 10 (C) could have occurred was the height difference caused by the situation that the device did not sit on a completely flat skin surface. For the future development of the device, an additional algorithm can be developed to allow the compensation for the issue caused by flatness. Also, the oxygen saturation equation we used in the algorithm was only calibrated with a simple calibration factor α, indicated in Equation (3), while a more complicated system may be employed to further calibrate the device. For instance, to account for the scattering of light, an additional light scattering constant can be included in Equation (3) to improve the result accuracy. In addition, the algorithm is unable to achieve real-time image visualization due to the delay of the calculation speed. To account for this issue, we can optimize the algorithm in the future or involve parallel processing. Another way to increase the processing speed is to reduce the resolution. The resolution was reduced from 720p to 300x300 pixel in order for better performance. However, lower resolution images result in even lower resolution of the mapping result.

Another issue of our designed device is that it prefers to work in a dark room. Any external light interference can potentially increase the noise level and reduce the accuracy of the result. The outside box provides cover for the device, and can reduce the incident light on some level. However, it cannot completely eliminate the outside light and can reflect additional light from its bottom layer. The device can also be further improved by a better user experience. We have considered multiple features to provide such experience and functions of the device, including GUI, user friendly rotary snobs for light intensity adjustment, etc., but there are some other ways to improve the device design. Currently, the device still needs to connect to an external screen; in the future, a touchable screen can be installed on the device to provide an easier control. What's more, the current pi camera cannot get high quality images and has rather high noise, it even produces occasional flickering that affects the final result. A camera with better quality can be used to gather better data for the analysis.

Overall, although the limitations and additional improvements are needed to be considered and implemented, the designed device, along with the current algorithms, succeeds in generating SaO_2 mapping and is prepared for the next stage for future commercialization into clinical and laboratory usage.

5.0 References

1. Ferlay J, Ervik M, Lam F, Colombet M, Mery L, Piñeros M, et al. Global Cancer Observatory: Cancer Today. *Lyon: International Agency for Research on Cancer*; 2020 (https://gco.iarc.fr/today, accessed February 2021).
2. Gwyther, S. J. Detection of Recurrent Cancer by Radiological Imaging. In General Methods and Overviews, Lung Carcinoma and Prostate Carcinoma; Hayat, M. A., Ed.; *Methods of Cancer Diagnosis, Therapy, and Prognosis*; Springer Netherlands: Dordrecht, 2008; pp 17–37.
3. Savelieva, Tatiana A.; Stratonnikov, Aleksander A.; Loschenov, Victor B. "Multi-spectral imaging of oxygen saturation." Proceedings of the SPIE, Volume 7022. (2008).
4. Brinkmann O, Wong DT. Salivary transcriptome biomarkers in oral squamous cell cancer detection. Adv Clin Chem.; 55:21-34, 2011
5. Goh, Yonggeng, et al. "Diagnostic Utility of Whole Body CT Scanning in Patients with Unexplained Weight Loss." *PLOS ONE*, vol. 13, no. 7, 2018, https://doi.org/10.1371/journal.pone.0200686.
6. Yossef Hay, Ohad, et al. "Pulse Oximetry with Two Infrared Wavelengths without Calibration in Extracted Arterial Blood." *Sensors*, vol. 18, no. 10, 2018, p. 3457., https://doi.org/10.3390/s18103457.
7. Chan, Edward D., et al. "Pulse Oximetry: Understanding Its Basic Principles Facilitates Appreciation of Its Limitations." *Respiratory Medicine*, vol. 107, no. 6, 2013, pp. 789–799., https://doi.org/10.1016/j.rmed.2013.02.004.
8. Townsend, Neil. "Pulse Oximetry." *Design and Implementation of Pulse Oximatry Based Computer* https://www.researchgate.net/publication/328891418_Design_And_Implementation_of_Pulse_Oximatry_Based_Computer_System.
9. GBD results tool. Seattle (WA): Institute for Health Metrics, University of Washington; 2020 (http://ghdx.healthdata.org/gbd-results-tool, accessed October 2021).
10. Huang, Z.; McWilliams, A.; Lui, H.; McLean, D. I.; Lam, S.; Zeng, H. Near-Infrared Raman Spectroscopy for Optical Diagnosis of Lung Cancer. *International Journal of Cancer* 2003, 107 (6), 1047–1052.
11. Odagiri, H.; Iizuka, T.; Kikuchi, D.; Kaise, M.; Takeda, H.; Ohashi, K.; Yasunaga, H. Gastrointestinal Endoscopy-Assisted Minimally Invasive Surgery for Superficial Cancer of the Uvula. *Clin Endosc* 2016, 49 (3), 289–293.
12. Cheng, Xuefeng, et al. "Breast cancer detection by mapping hemoglobin concentration and oxygen saturation." Appl Opt. 42(31):6412-21, 2003
13. "MRI." *CancerQuest*, https://www.cancerquest.org/patients/detection-and-diagnosis/magnetic-resonance-imaging-mri.
14. Sun Zheng, Han Duoduo, Yuan Yuan,"2-D image reconstruction of photoacoustic endoscopic imaging based on time-reversal,Computers in Biology and Medicine." Volume 76, 2016, Pages 60-68, https://doi.org/10.1016/j.compbiomed.2016.06.028.
15. Aoyagi, Takuo, et al. "Multiwavelength Pulse Oximetry: Theory for the Future." *Anesthesia & Analgesia*, vol. 105, no. 6, 2007, https://doi.org/10.1213/01.ane.0000268716.07255.2b.
16. Igarashi, Hiroshi, et al. "Oxygen Use and Survival in Patients with Advanced Cancer and Low Oxygen Saturation in Home Care: A Preliminary Retrospective Cohort Study." *BMC Palliative Care*, vol. 19, no. 1, 2020, https://doi.org/10.1186/s12904-019-0511-9.
17. Christen, T.; Bouzat, P.; Pannetier, N.; Coquery, N.; Moisan, A.; Lemasson, B.; Thomas, S.; Grillon, E.; Detente, O.; Rémy, C.; Payen, J.-F.; Barbier, E. L. Tissue Oxygen Saturation Mapping with Magnetic Resonance Imaging. J Cereb Blood Flow Metab 2014, 34 (9), 1550–1557.
18. Gallez, B. Oxygenation Status in Normal Tissues, Pathological Tissues and Malignant Tumors: A PO2 Database Based on Electron Paramagnetic Resonance (EPR) Oximetry Measurements. *Applied Magnetic Resonance* 2021.
19. Hettie, K. S.; Klockow, J. L.; Moon, E. J.; Giaccia, A. J.; Chin, F. T. A NIR Fluorescent Smart Probe for Imaging Tumor Hypoxia. *Cancer Reports*, e1384.
20. Jean-Pierre, P. Integrating Functional Near-Infrared Spectroscopy in the Characterization, Assessment, and Monitoring of Cancer and Treatment-Related Neurocognitive Dysfunction. *NeuroImage* 2014, 85, 408–414.
21. Jiang, S.; Pogue, B. W.; McBride, T. O.; Paulsen, K. D. Quantitative Analysis of Near-Infrared Tomography: Sensitivity to the Tissue-Simulating Pre Calibration Phantom. *J Biomed Opt* 2003, 8 (2), 308–315.
22. Marcos-Vidal, A.; Vaquero, J. J.; Ripoll, J. Optical Properties of Tissues in the Near Infrared: Their Relevance for Optical Bioimaging. In *Near Infrared-Emitting Nanoparticles for Biomedical Applications*;

Benayas, A., Hemmer, E., Hong, G., Jaque, D., Eds.; Springer International Publishing: Cham, 2020; pp 1–20.
23. Walsh, J. C.; Lebedev, A.; Aten, E.; Madsen, K.; Marciano, L.; Kolb, H. C. The Clinical Importance of Assessing Tumor Hypoxia: Relationship of Tumor Hypoxia to Prognosis and Therapeutic Opportunities. *Antioxidants & Redox Signaling* 2014, 21 (10), 1516–1554.
24. Le V. N. Du, et al. Calibration of Spectral Imaging Devices With Oxygenation-Controlled Phantoms: Introducing a Simple Gel-Based Hemoglobin Model. “Frontiers in Physics.” https://www.frontiersin.org/article/10.3389/fphy.2019.00192. 2296-424X
25. Krauter, P., Nothelfer, S., Bodenschatz, N., Simon, E., Stocker, S., Foschum, F., & Kienle, A. (2015). Optical phantoms with adjustable subdiffusive scattering parameters. *Journal of Biomedical Optics*, *20*(10), 105008. https://doi.org/10.1117/1.jbo.20.10.105008
26. Bosschaart, N., Edelman, G. J., Aalders, M. C., van Leeuwen, T. G., & Faber, D. J. (2014). A literature review and novel theoretical approach on the optical properties of whole blood. *Lasers in medical science*, 29(2), 453–479. https://doi.org/10.1007/s10103-013-1446-7
27. Peterson, B. K. (2009). *Vital signs*. Physical Rehabilitation. https://www.sciencedirect.com/science/article/pii/B9780721603612500259
28. *Raspberry Pi Documentation*. https://www.raspberrypi.com/documentation/accessories/camera.html
29. *A SUPERVISED SIGNAL-TO-NOISE RATIO ESTIMATION OF SPEECH SIGNALS*. Web of science. (n.d.). Retrieved May 2, 2022, from https://www.webofscience.com/wos/woscc/full-record/WOS:000758478600006